Encapsulating Fe_2O_3 Nanotubes into Carbon-Coated Co_9S_8 Nanocages Derived from a MOFs-Directed Strategy for Efficient Oxygen Evolution Reactions and Li-Ions Storage

Shoushuang Huang, Zhiqiang Jin, Yanwei Ding, Ping Ning, Qiaochuan Chen,* Jie Fu, Qian Zhang, Jie Zhang, Peijun Xin, Yong Jiang,* and Zhangjun Hu*

The development of high-efficiency, robust, and available electrode materials for oxygen evolution reaction (OER) and lithium-ion batteries (LIBs) is critical for clean and sustainable energy system but remains challenging. Herein, a unique yolk–shell structure of Fe_2O_3 nanotube@hollow Co_9S_8 nanocage@C is rationally prepared. In a prearranged sequence, the fabrication of Fe_2O_3 nanotubes is followed by coating of zeolitic imidazolate framework (ZIF-67) layer, chemical etching of ZIF-67 by thioacetamide, and eventual annealing treatment. Benefiting from the hollow structures of Fe_2O_3 nanotubes and Co_9S_8 nanocages, the conductivity of carbon coating and the synergy effects between different components, the titled sample possesses abundant accessible active sites, favorable electron transfer rate, and exceptional reaction kinetics in the electrocatalysis. As a result, excellent electrocatalytic activity for alkaline OER is achieved, which delivers a low overpotential of 205 mV at the current density of 10 mA cm^{-2} along with the Tafel slope of 55 mV dec^{-1}. Moreover, this material exhibits excellent high-rate capability and excellent cycle life when employed as anode material of LIBs. This work provides a novel approach for the design and the construction of multifunctional electrode materials for energy conversion and storage.

1. Introduction

Serious environmental pollution and energy crisis are prompting people to focus on renewable and clean energies, new technologies and devices associated with energy storage and conversion systems.[1] Particularly, water splitting for hydrogen production and lithium-ion batteries (LIBs) are considered ideal solutions for achieving energy conversion and storage in a sustainable way.[2] Nowadays, the key challenges of using these technologies and devices lie in the developments of more efficient and stable electrode materials. For the electrochemical water splitting, due to the high overpotential and intrinsically sluggish reaction kinetics of the oxygen evolution reaction (OER), low-cost, high efficiency and stable earth-abundant electrocatalysts are required to enhance the energy conversion efficiency.[3] Similarly, the commercial graphite anode materials for LIBs have limited inherent theoretical capacity ($\approx$372 mAh g^{-1}), which cannot meet the requirements of high energy density batteries for rapidly growing smartphone, electrical vehicles, and aerospace applications. How to further improve the energy density of LIBs faces great challenges. Therefore, it is urgent to invent competitive multifunctional electrode nanomaterials with suitable components and architectures for highly efficient OER electrocatalysts and high-performance LIBs.

Recently, iron-based oxides have been widely studied in the fields of energy storage and conversions owing to their high electrochemical activity, rich redox properties, natural abundance, and simple preparation.[4] However, the electrocatalytic activity of Fe-based oxides is highly dependent on their

S. Huang, Z. Jin, Y. Ding, P. Ning, J. Fu, Q. Zhang, J. Zhang, P. Xin, Y. Jiang, Z. Hu
School of Environmental and Chemical Engineering
Shanghai University
99 Shangda Road, Shanghai 200444, P. R. China
E-mail: jiangyong@shu.edu.cn

Q. Chen
School of Computer Engineering and Science
Shanghai University
99 Shangda Road, Shanghai 200444, P. R. China
E-mail: qcchen@shu.edu.cn

Z. Hu
Division of Molecular Surface Physics and Nanoscience
Department of Physics
Chemistry and Biology
Linköping University
Linköping 58183, Sweden
E-mail: zhangjun.hu@liu.se

electronic structure and surface energy. The low conductivity and specific surface area of Fe-based oxides make them difficult to be used as OER catalysts directly. As the anode electrode of LIBs, Fe-based oxides often suffer from large volume changes during the charge/discharge process, resulting in rapid attenuation of specific capacity and poor cycling life.[5] One generally accepted approach to alleviate these problems is to incorporate Fe-based oxides with other highly active materials. For example, the hierarchical Fe_2O_3@Ni_3Se_4 nanotubes prepared by Zheng et al. exhibited much better OER and lithium storage performance than the individual Fe_2O_3 and Ni_3Se_4.[6] The enhanced OER electrocatalytic activity was attributed to the short diffusion pathways, sufficient active sites and synergistic effects between the Ni_3Se_4 and Fe_2O_3, whereas the improved lithium storage performance was ascribed to the high specific capacity of Fe_2O_3 and fast electron transportation of Ni_3Se_4. Suryanto et al. found that the Janus $Ni–Fe_2O_3$ nanoparticle catalyst displayed enhanced OER catalytic activity induced by the electronic coupling effect between Ni and γ-Fe_2O_3 at the interface.[7] The flower-like FeS/Fe_2O_3 composite synthesized by Wang et al. also manifested higher specific capacity and better cycling stability compared with pure FeS and Fe_2O_3.[8] Additionally, cobalt sulfides are promising electrode materials in the fields of electrocatalysis, Li(Na)-ions batteries, sensing, and solar cells, because of their high conductivity and unique physical and chemical properties.[9] Therefore, it is reasonably expected that the electrode materials consisted of iron oxide and cobalt sulfide perform well as OER catalyst and LIBs anode.

In addition to preparing composite materials, another common way is to construct delicate nanostructures with short ion diffusion paths and enlarged surface areas. Particularly, the yolk–shell structure exhibits remarkable potential applications in OER and LIBs, drawing special interests.[10] Specifically, the favorable porous texture can benefit the electrocatalysis performance because of sufficient electrode–electrolyte contact area, better electrolyte penetration, and an extremely reduced path for gas diffusions. For instance, Xu et al. reported that the α-Fe_2O_3 yolk–shell microspheres displayed good OER catalytic activity with a low overpotential of 275 mV.[11] Ganesan et al. found that the CoP_2/Fe-CoP_2 yolk–shell nanoboxes manifested better OER activity as compared to Fe–CoP and CoP with similar morphology.[12] At the same time, the well-defined interior voids in the yolk–shell structure can effectively accommodate the structural strain and ensure facile Li^+ ion diffusion. Based on the above studies, it seems logical to envision that the construction of an elaborate yolk–shell architecture can further improve the electrochemical performance of the multifunctional electrode nanomaterials composed of iron oxide and cobalt sulfide.

Up to now, many strategies have been developed to fabricate a yolk–shelled framework.[13] However, most of the reported template-assisted methods are time-consuming and/or material-wasteful. Metal–organic frameworks (MOFs) have great potentials in the preparation of materials for energy storage and conversion because of their controllable advantages on the homogeneous morphologies, small sizes, porous structures, and large specific surface areas.[14] Herein, a well-defined yolk–shell structure of Fe_2O_3@h-Co_9S_8@C is rationally designed and produced via engineering a Fe_2O_3 nanotube@ZIF-67 core–shell structure followed by chemical etching/anion exchange and carbonization at high temperature in sequence. The as-synthesized Fe_2O_3@h-Co_9S_8@C possesses abundant accessible active sites, favorable ionic transfer rate, and exceptional reaction kinetics, which are beneficial for both OER and LIBs. Impressively, it exhibited small overpotentials of 205 and 281 mV for OER at catalytic current densities of 10 and 100 mA cm^{-2} in 1 M KOH electrolyte, respectively. When employed as anode materials for LIBs, it maintains a reversible capacity of 570.8 mAh g^{-1} at 1.0 A g^{-1} after 100 cycles, and delivers a capacity of 445.2 mAh g^{-1} even at the current density of 4.0 A g^{-1}.

2. Results and Discussion

2.1. Material Preparation and Characterization

The synthesis of Fe_2O_3@h-Co_9S_8@C yolk–shell structure mainly contained three steps, as schematically illustrated in **Figure 1**. First, uniform hollow Fe_2O_3 nanotubes were prepared via a coordination-assisted dissolution process according to previous work. Subsequently, the as-obtained Fe_2O_3 nanotubes were employed as seeds for the crystallization of the ZIF-67 layer, rendering a well-defined Fe_2O_3@ZIF-67 core–shell nanoparticle. Following that, the as-formed Fe_2O_3@ZIF-67 nanoparticles were homogeneously dispersed in an isopropanol solution of thioacetamide (TAA) with stirring for 12 h at room temperature. During this process, abundant sulfide ions were produced owing to the decomposition of TAA. These sulfide ions reacted with the Co^{2+} cations dissolving from the surface of the ZIF-67 particles, leading to the formation of an amorphous Co–S shell (a-CoS) around the scaffold of each ZIF-67 particle. By precisely controlling the amount of TAA, the ZIF-67 template can be completely converted into a-CoS nanocage.
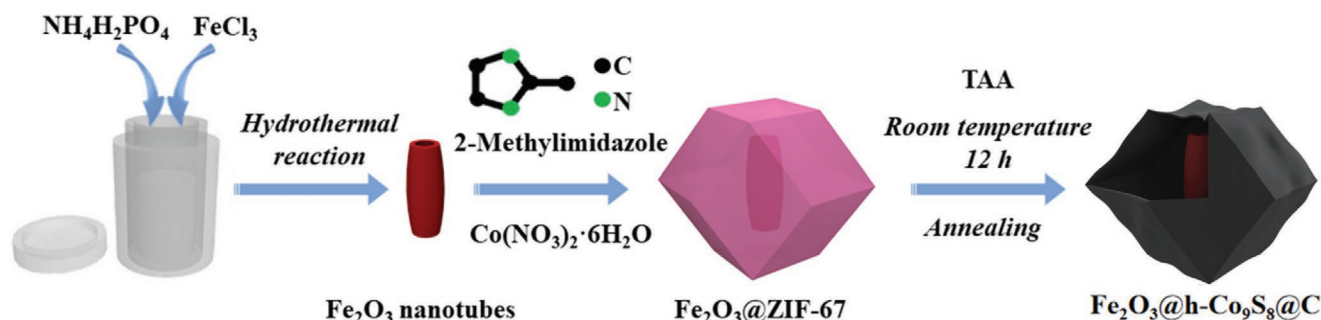

Figure 1. Schematic illustration of the synthesis of Fe_2O_3@h-Co_9S_8@C structure.
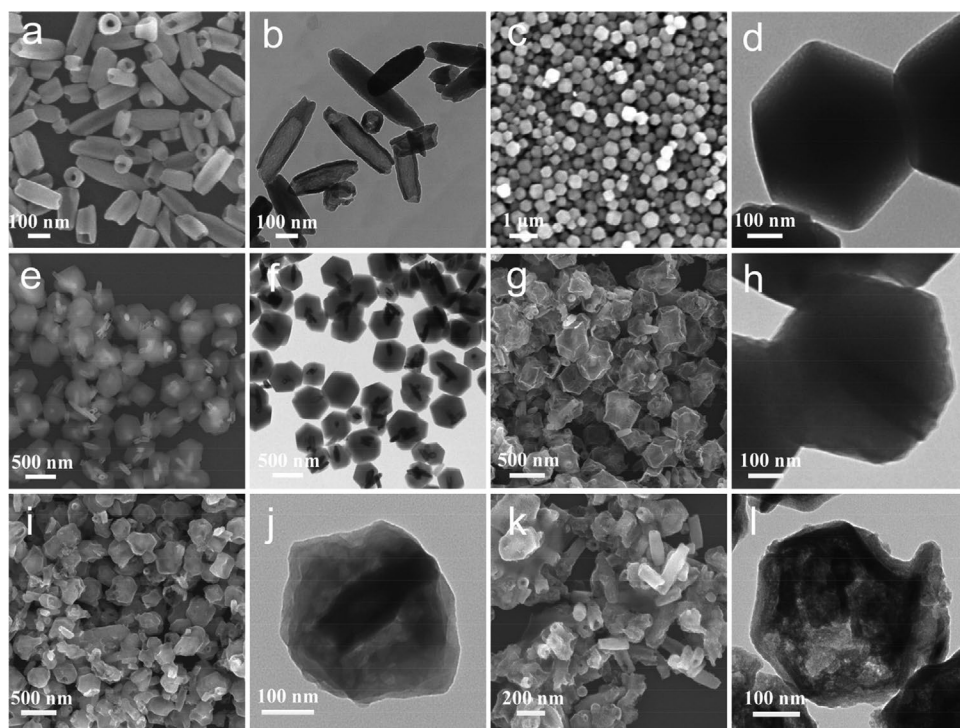
2103178 (2 of 10)

Figure 2. SEM (a,c,e,g,i,k) and TEM (b,d,f,h,j,l) images of the as-synthesized Fe_2O_3 nanotube (a, b), ZIF-67 (c,d), Fe_2O_3@ZIF-67 (e,f), Fe_2O_3@ZIF-67@Co_9S_8@C (g,h), Fe_2O_3@h-Co_9S_8@C (i,j), and Fe_2O_3@c-Co_9S_8@C (k,l).

Finally, the amorphous a-CoS was converted to Co_9S_8 nanocage by a temperature-controlled thermal annealing treatment. Meanwhile, the organic skeleton originating from ZIF-67 is converted to a carbon layer that coated on the surface of Co_9S_8 nanocages simultaneously (Figure S1, Supporting Information). As a result, the nearly uniform and monodispersed Fe_2O_3@h-Co_9S_8@C nanoparticles with a well-defined yolk–shell structure were obtained.

The morphology details and crystal structure of the samples were investigated by scanning electron microscope (SEM) and transmission electron microscope (TEM) observations. The SEM image in **Figure 2**a shows that the as-prepared Fe_2O_3 nanotubes have a diameter of about 100 nm and a length of 250–400 nm. The corresponding TEM image confirms that the Fe_2O_3 nanotubes present a hollow texture (Figure 2b). The SEM image in Figure 2c indicates that the ZIF-67 nanoparticles have a uniform polyhedral morphology with an average size of 225 nm. Different from that of hollow Fe_2O_3 nanotubes, the TEM image in Figure 2d implies that the ZIF-67 nanoparticles are solid with a smooth surface. To prepare the Fe_2O_3@ZIF-67 core–shell structure, the as-prepared Fe_2O_3 nanotubes were added into the methanol solution containing $Co(NO_3)_2$, 2-methylimidazole, and polyvinyl pyrrolidone (PVP). Due to the strong coordination interactions between pyrrolidone rings (C=O) and Co^{2+}, the Co^{2+} is easily adsorbed on the surface of PVP-caped Fe_2O_3 nanotubes.[15] Subsequently, the Co^{2+} coordinated with 2-methylimidazole ligands to generate ZIF-67 nanoparticles. These ZIF-67 nanoparticles were coated on the surface of Fe_2O_3 nanotubes, rendering a well-defined Fe_2O_3@ZIF-67 core–shell heterostructure. As presented in the SEM image of Figure 2e, ZIF-67 was formed and assembled into a shell uniformly covering the surface of the Fe_2O_3 nanotubes. The TEM images in

Figure 2f confirm that the product of Fe_2O_3@ZIF-67 presents a core–shell morphology with a core of Fe_2O_3 nanotube and a shell of ZIF-67. Moreover, to obtain a high-quality Fe_2O_3@ZIF-67 core–shell structure, the amount of Fe_2O_3 needs to be controlled precisely (Figure S2, Supporting Information).

It was found that the amount of TAA played an important role in the composite and morphology of the ZIF-67 templates, which subsequently affected the morphology, composition, and electrochemical performance of the Fe_2O_3@Co_9S_8@C products. By carefully controlling the amounts of TAA during the sulfidation reaction, different Fe_2O_3@Co_9S_8@C nanocomposites were obtained. When the amount of TAA was 1 mmol, the field emission scanning electron microscopy (FESEM) and TEM images illustrate that the overall polyhedral-like appearance of the as-obtained product is well inherited (Figure 2g). However, the diffraction peaks of ZIF-67 have still presented in the X-ray diffraction (XRD) patterns (Figure S3, Supporting Information), indicating that ZIF-67 is not thoroughly transformed into Co–S compounds during the chemical corrosion processes. The TEM image in Figure 2h suggests that the sample still presents a solid construction, and closer inspection reveals that the surface of ZIF-67 becomes rather rough, evidencing the occurrence of sulfidation reaction.[16]

These results imply that the sample consists Fe_2O_3 nanotubes, ZIF-67, and a trace amount of carbon-coated Co_9S_8 (named as Fe_2O_3@ZIF67@Co_9S_8@C). Notably, no distinct XRD diffraction peaks of Co_9S_8 could be found in the product, which might be due to its low crystallinity and content. Increasing the amount of TAA to 2 mmol, the original external metal–organic framework of ZIF-67 was completely etched, which were converted into hollow carbon-coated Co_9S_8 nanocages after annealing treatment. The SEM in Figure 2i shows that the hollow Co_9S_8 nanocage well
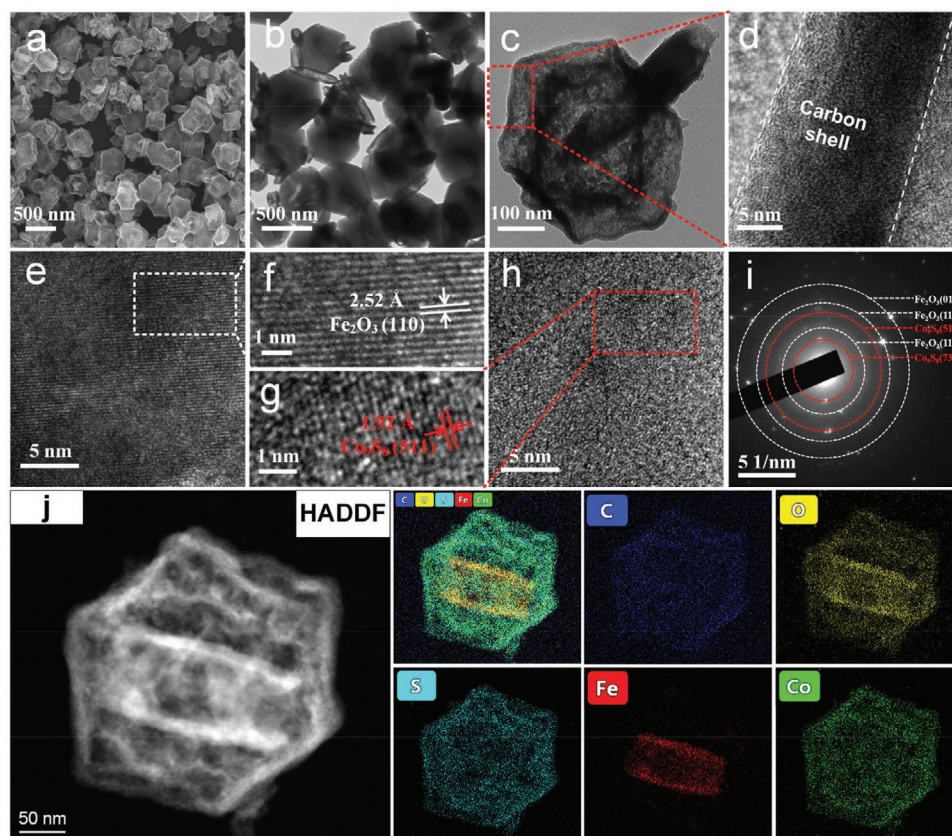
Figure 3. a) SEM, b,c) TEM, d–h) high-resolution TEM images, i) SAED, j) element mapping images of Fe_2O_3@h-Co_9S_8@C sample, respectively.

inherits the polyhedral morphology and dimensions of ZIF-67 templates but with a rough surface. Additionally, the TEM analysis in Figure 2j further identifies the presence of Fe_2O_3 cores inside hollow carbon-coated Co_9S_8 shells by forming a yolk–shell structure of Fe_2O_3 nanotube@hollow Co_9S_8 nanocage@C (Fe_2O_3@h-Co_9S_8@C). Further increasing the amount of TAA to 3 mmol, the SEM and TEM images in Figure 2k,l indicate that some of the external Co_9S_8 shells break into pieces and the internal Fe_2O_3 nanotubes are free in space, forming a multiple core–shell structure of Fe_2O_3 nanotube@cracked-Co_9S_8 nanocage@C (Fe_2O_3@c-Co_9S_8@C). The structural breakdown of Co_9S_8 nanocages can be ascribed to the excessive chemical corrosion of TAA, in accordance with previous reports.[17]

The morphology details and lattice fringes of the Fe_2O_3@h-Co_9S_8@C were further investigated by SEM and TEM analysis. As shown in **Figure 3**a, the Fe_2O_3@h-Co_9S_8@C still maintains a dodecahedral shape, but its shell is slightly wrinkled. The TEM images of Figure 3b,c indicate that the Fe_2O_3 nanotubes are encapsulated by carbon-coated Co_9S_8 nanocages. The typical thickness of carbon layer is about 15.7 nm (Figure 3d). The high-resolution TEM images are displayed in Figure 3e–h, the lattice fringes with distances of 2.52 and 1.92 Å correspond to the (110) planes of Fe_2O_3 and the (511) planes of Co_9S_8, respectively. The etched defect-rich surface of Co_9S_8 is beneficial to the dissociative adsorption of water molecules, further boosts the ability of oxygen evolution (Figure S4, Supporting Information). The selected area electron diffraction (SAED) pattern exhibits a series of clear polycrystalline diffraction rings (Figure 3i), corresponding to (012),

(110), (116) lattice planes of Fe_2O_3 and (511), (731) lattice plane of Co_9S_8, respectively. The elemental mapping images were taken from the region of the high-angle annular dark-field images. As shown in Figure 3j, Co, S, and C elements uniformly distribute throughout the particle, while Fe and O atoms are inclined to be localized in the isolated central regions rather than distributed in the whole area, revealing that Fe_2O_3 nanotubes are completely embedded in carbon-coated Co_9S_8 nanocages. The Raman spectroscopy test was also carried out to get more information of the carbon layer in the sample. The peaks in Figure S5 of the Supporting Information at 1300 and 1580 cm^{-1} correspond to the defect-induced structures of carbon (D band) and graphitic carbon (G band), respectively, confirming the existence of low crystallinity carbon. The composition of Fe_2O_3 and Co_9S_8 in the Fe_2O_3@h-Co_9S_8@C was studied by inductively coupled plasma optical emission spectrum (ICP-OES). The results reveal that the weight contents of Fe and Co are 30.0 and 17.7 wt%, respectively (Table S1, Supporting Information).

The XRD patterns of the as-prepared Fe_2O_3, ZIF-67, Fe_2O_3@ZIF-67, and Fe_2O_3@h-Co_9S_8@C samples are displayed in **Figure 4**a. The diffraction peaks at 2 theta angles of 24.1°, 33.1°, 35.6°, 40.8°, 49.5°, 54.1°, 62.4°, and 64.0° can be classified as (012), (104), (110), (113), (024), (116), (214), and (300) planes of Fe_2O_3 (JCPDS No. 33-0664), respectively. The XRD profile of the Fe_2O_3 nanotube exhibits sharp diffraction peaks, indicating its fine crystallinity. The diffraction peaks of ZIF-67 are consistent with previous reports, suggesting its high purity.[18] For the Fe_2O_3@ZIF-67 sample, the diffraction peaks of Fe_2O_3
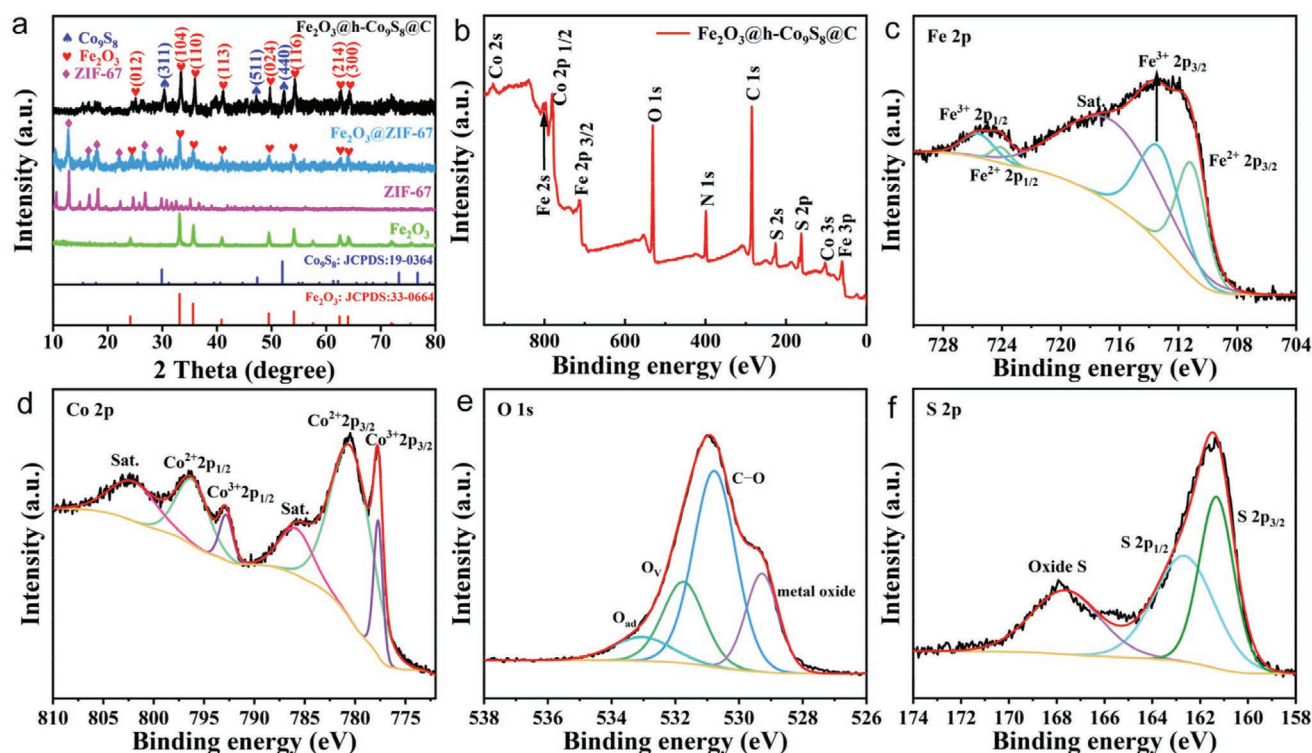
Figure 4. a) XRD patterns of the Fe_2O_3, ZIF-67, Fe_2O_3@ZIF-67, and Fe_2O_3@h-Co_9S_8@C samples. b) Survey spectra, c) Fe 2p, d) Co 2p, e) O 1s, and f) S 2p XPS spectra of the as-obtained Fe_2O_3@h-Co_9S_8@C.

and ZIF-67 can also be observed, indicating the successful synthesis of Fe_2O_3@ZIF-67 nanocomposites. For the XRD pattern of Fe_2O_3@h-Co_9S_8@C, the diffraction peaks of Fe_2O_3 still exist, however, the characteristic peaks of ZIF-67 disappear, and some new diffraction peaks belonging to Co_9S_8 emerge. Particularly, the diffraction peaks at 2 theta angles of 29.9°, 51.9°, and 63.9° can be attributed to the (311), (511), and (440) crystal surfaces of Co_9S_8 (JCPDS No. 19–0364), respectively. The results reveal that the Fe_2O_3@ZIF-67 sample can be successfully converted to Fe_2O_3@Co_9S_8@C through the controlled sulfurization and annealing treatment.

X-ray photoelectron spectroscopy (XPS) measurement was carried out to investigate the chemical environment and element valence of Fe_2O_3@h-Co_9S_8@C. The XPS survey spectra in Figure 4b suggest the existence of C, Fe, O, Co, S, and N in the sample. As exhibited in Figure 4c, the peaks at 711.2, 713.6, 724.1, and 725.7 eV can be ascribed to the Fe^{2+} $2p_{3/2}$, Fe^{3+} $2p_{3/2}$, Fe^{2+} $2p_{1/2}$, and Fe^{3+} $2p_{1/2}$, respectively, implying the existence of both ferrous and ferric states.[19] The peaks at the binding energy of 717.4 eV correspond to the satellite peaks. The high-resolution XPS of Co spectrum is presented in Figure 4d, in which peaks can be divided into two spin–orbit doublets and two shakeup satellite peaks. The first doublet is at 780.7 eV (Co^{2+} $2p_{3/2}$) and 796.4 eV (Co^{2+} $2p_{1/2}$), along with the second doublet at 777.7 eV (Co^{3+} $2p_{3/2}$) and 792.8 eV (Co^{3+} $2p_{1/2}$).[20] The oxygen binding energy of 529.3, 530.8, and 533.1 eV in Figure 4e is attributed to lattice oxygen in metal oxide, C—O bond and adsorbed water, respectively.[21] The S 2p XPS spectrum (Figure 4f) is also analyzed to figure out the valence state of sulfur. The peaks at 161.7 and 162.7 eV correspond to the S $2p_{3/2}$ and S $2p_{1/2}$ orbitals of Co_9S_8, respectively.

Besides, the peak at 168.7 eV can be attributed to the SO_x groups formed by the inevitable oxidation of S in the air.[22]

2.2. Electrocatalytic Performance toward OER

In order to explore the feasibility of the prepared materials in OER application, corresponding tests were established with a standard three-electrode system. The obtained linear sweep voltammetry (LSV) plots of each catalyst are depicted in **Figure 5**a. It can be seen that the Fe_2O_3 nanotubes manifest poor alkaline OER activity owing to its intrinsic low catalytic activity and limited catalytic sites, with a high overpotential (η_{10}) of 353 mV at 10 mA cm^{-2}. By contrast, the Fe_2O_3-based hybrid catalysts exhibit better OER performance. Particularly, the Fe_2O_3@h-Co_9S_8@C displays an impressive OER activity with a low η_{10} of 205 mV, exceeding those of Fe_2O_3@ZIF-67@Co_9S_8@C (234 mV), Fe_2O_3@c-Co_9S_8@C (286 mV), Co_9S_8@C (256 mV), ZIF-67 (338 mV), and Fe_2O_3@ZIF-67 (332 mV). These results reveal that the construction of yolk–shell structure can effectively improve the electrocatalytic performance of the materials. For comparison, the LSV curve without iR compensation is also provided in Figure S6 of the Supporting Information. Compared with the recent similar catalysts and other advanced catalysts (Table S1, Supporting Information), the OER activity of Fe_2O_3@h-Co_9S_8@C is comparable to even better than most iron-based oxides and cobalt-based sulfides. The enhanced OER activity of Fe_2O_3@h-Co_9S_8@C can be attributed to the enlarged catalytic active sites, improved conductivity and the coupling effect between different composites.
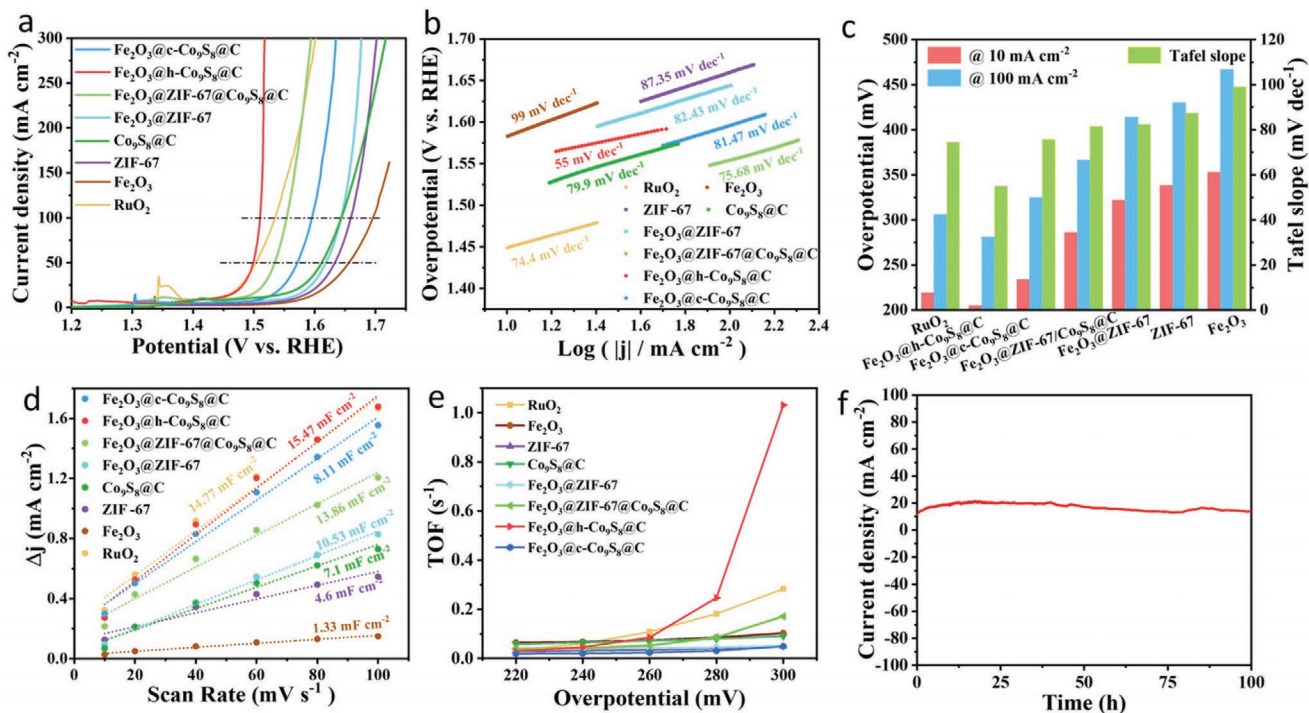
Figure 5. Electrochemical measurements for the OER in 1 M KOH solution with a scan rate of 5 mV s^{-1}. a) LSV curves, b) Tafel plots, c) the summary of η_{10}, η_{100}, and Tafel slopes, d) fitted C_{dl} and e) TOF values of the as-synthesized RuO$_2$, Fe$_2$O$_3$, ZIF-67, Co$_9$S$_8$@C, Fe$_2$O$_3$@ZIF-67, Fe$_2$O$_3$@ZIF-67@Co$_9$S$_8$@C, Fe$_2$O$_3$@h-Co$_9$S$_8$@C, and Fe$_2$O$_3$@c-Co$_9$S$_8$@C samples. f) Chronoamperometric plot of Fe$_2$O$_3$@h-Co$_9$S$_8$@C at the potential of 220 mV (vs RHE).

Another vital metric to assess the electrochemical property is the Tafel plot, which can be acquired by fitting the polar curve with the Tafel equation:[23] $\eta = b \log j + c$, where η is the overpotential, b is the slope, j is the current density, and c is the constant. Generally, the lower the Tafel slope is, the higher the catalytic activity of the catalyst has.[24] The Tafel slope of polarization curves for the as-prepared catalysts are shown in Figure 5b. The Fe$_2$O$_3$@h-Co$_9$S$_8$@C catalyst manifest a Tafel slope of 55 mV dec^{-1}, much smaller than those of Fe$_2$O$_3$ (99 mV dec^{-1}), ZIF-67 (87.35 mV dec^{-1}), Co$_9$S$_8$@C (79.9 mV dec^{-1}), Fe$_2$O$_3$@ZIF-67 (82.43 mV dec^{-1}), Fe$_2$O$_3$@ZIF-67@Co$_9$S$_8$@C (75.68 mV dec^{-1}), Fe$_2$O$_3$@c-Co$_9$S$_8$@C (81.47 mV dec^{-1}), and RuO$_2$ (74.4 mV dec^{-1}), respectively. The Tafel slope and overpotential of materials are summarized in Figure 5c for further comparison. The smallest overpotential and Tafel slope illustrate that the Fe$_2$O$_3$@h-Co$_9$S$_8$@C had the fastest OER kinetics and catalytic performance.

To get insights into the origin of the high electrocatalytic activity of Fe$_2$O$_3$@h-Co$_9$S$_8$@C, electrochemically active surface area (ECSA) was calculated through the formula:[25] ECSA = C_{dl}/C_S, where C_S is the specific capacitance, commonly is 0.040 mF cm^{-2} in the electrolyte of 1 M NaOH solution, C_{dl} is double layer capacitance acquired from cyclic voltammetry (CV) curves. CV cycle plots at different sweeping speeds were tested in the potentials of non-Faradaic current response range for each catalyst. According to CV cycle curves (Figures S7 and S8, Supporting Information), the current density difference value (ΔJ) at the potential of 1.18 V was plotted against the series sweeping values, and the slope of the fitted curve is

twice of the C_{dl}. As shown in Figure 5d, the C_{dl} for Fe$_2$O$_3$@h-Co$_9$S$_8$@C is 15.47 mF cm^{-2}, much larger than those of RuO$_2$ (14.77 mF cm^{-2}), Fe$_2$O$_3$ (1.33 mF cm^{-2}), ZIF-67 (4.6 mF cm^{-2}), Co$_9$S$_8$@C (7.1 mF cm^{-2}), Fe$_2$O$_3$@ZIF-67 (10.53 mF cm^{-2}), Fe$_2$O$_3$@ZIF-67@Co$_9$S$_8$@C (13.86 mF cm^{-2}), and Fe$_2$O$_3$@c-Co$_9$S$_8$@C (8.11 mF cm^{-2}). The larger C_{dl} value implies that the Fe$_2$O$_3$@h-Co$_9$S$_8$@C catalyst has considerable exposed active sites. To evaluate the intrinsic OER activity of different catalysts, the OER polarization curves are normalized with the calculated ECSA value. As shown in Figure S9 of the Supporting Information, the plot maintained the original growing trend and the overpotential of Fe$_2$O$_3$@h-Co$_9$S$_8$@C is still smaller than the other electrodes, confirming that the intrinsic activity of Fe$_2$O$_3$@h-Co$_9$S$_8$@C is indeed better than the controlled samples. The hollow core and shell supplies numerous easily accessible active sites for catalytic reaction, and the partially exposed Fe$_2$O$_3$ increases channels for gas spillage during the OER process.

Turnover frequency (TOF) is the conversion number of a single active site per unit time, which can be used as an important indication to reveal the catalytic reaction rate and intrinsic activity of the catalyst. It can be seen from Figure 5e that the TOF value of Fe$_2$O$_3$@h-Co$_9$S$_8$@C is 1.0310 s^{-1} at the potential of 300 mV, much higher than Fe$_2$O$_3$@ZIF-67 (0.0513 s^{-1}), ZIF-67 (0.0497 s^{-1}), Co$_9$S$_8$@C (0.0909 s^{-1}), Fe$_2$O$_3$@c-Co$_9$S$_8$@C (0.04928 s^{-1}), Fe$_2$O$_3$@ZIF-67@Co$_9$S$_8$@C (0.17155 s^{-1}), and RuO$_2$ (0.2828 s^{-1}), respectively. The Fe$_2$O$_3$@h-Co$_9$S$_8$@C has the largest TOF, suggesting it has the best OER catalytic activity. In addition to catalytic activity, the stability of the catalyst is a crucial parameter to evaluate the OER property of the material.

**ADVANCED
SCIENCE NEWS**

www.advancedsciencenews.com

**NANO · MICRO
small**

www.small-journal.com

As depicted in Figure 5f, the stability of the Fe_2O_3@h-Co_9S_8@C catalyst was tested by the chronoamperometry method. The current density increases by about 10 mA cm^{-2} in the test after 20 h and basically maintains at about 17 mA cm^{-2} under constant 0.22 V potential for 100 h. This result indicates that the Fe_2O_3@h-Co_9S_8@C catalyst possesses excellent OER durability in alkaline solution.

In order to investigate the morphology, structure, and composition changes of Fe_2O_3@h-Co_9S_8@C after OER test, XPS, SEM, and XRD measurements were carried out. The chemical environment and element valence of Fe_2O_3@h-Co_9S_8@C after the OER test are first explored by XPS. As exhibited in Figure S10a of the Supporting Information, the original Fe^{2+} 2p3/2 and Fe^{3+} 2p3/2 peaks at 711.2 and 713.6 eV shifted to 711.8 and 714.2 eV, respectively, which corresponds to the phase change of Fe_2O_3 to FeOOH.[26] The high-resolution XPS of Co spectrum in Figure S10b of the Supporting Information reveals that the Co^{3+} is disappeared after OER cycling, suggesting the Co_9S_8 on the surface has been converted to CoO.[27] Meanwhile, the peaks of S 2p$_{1/2}$ and S 2p$_{1/2}$ disappear in Figure S10c of the Supporting Information, which is consistent with the conclusion that the Co_9S_8 on the surface has been converted to CoO. The XPS of O spectrum is also investigated in Figure S10d of the Supporting Information, the peak of defect oxides in O 1s spectra located at 531.8 eV disappears after the OER test, which may be due to the collapse of oxygen vacancy during the oxygen evolution progress. The emerging oxygen peak of 535.2 eV (O–F) is attributed to Nafion used in the test progress[28] Based on these results, it can be referred that the Co_9S_8 on the surface layer of nickel foam has been transformed into an active CoO

phase. The SEM image of Fe_2O_3@h-Co_9S_8@C sample after 12 h OER cycling was shown in Figure S11 of the Supporting Information. It can be seen that the surface of Fe_2O_3@h-Co_9S_8@C was deformed due to the inevitable phase change and volume change of Co_9S_8. However, the overall morphology can still be well retained. XRD measurement was also carried out to investigate whether the crystal structure of the post-OER catalyst has changed. As shown in Figure S12 of the Supporting Information, the strong peaks located at 44.7°, 52.1°, and 76.7° are attributed to the diffraction peaks of nickel foam substrate. Whereas, the peaks of Fe_2O_3 keep unchanged basically. The XRD peak intensity of Co_9S_8 is obviously decreased, implying that the content of Co_9S_8 in the nanocomposite is reduced after the long-term OER process.[29]

2.3. Electrochemical Performance toward Lithium-Ion Batteries

Figure 6a displays the initial five cycles of cyclic voltammetry curve for the Fe_2O_3@h-Co_9S_8@C electrode at a scan rate of 0.1 mV s^{-1} in the potential window of 0.01 to 3.00 V. The obvious reduction peaks around 0.68 V in the first cycle (Figure 6a; Figure S13a, Supporting Information) ascribes to the reduction of Fe^{3+}/Fe^{2+} and Fe^{2+}/Fe^0 along with the formation of metallic Fe and Li_2O.[30] The reduction peaks around 1.71 and 1.30 V are same as the reduction peaks of Co_9S_8@C (shown in Figure S13b, Supporting Information), corresponding to the reduction of Co_9S_8/$Li_xCo_9S_8$ and $Li_xCo_9S_8$/Co^0, respectively.[9d] Correspondingly, there are two couples of oxidation peaks range from 1.5 to 2.5 V, which attributes to the oxidation of Fe^0/Fe^{3+}
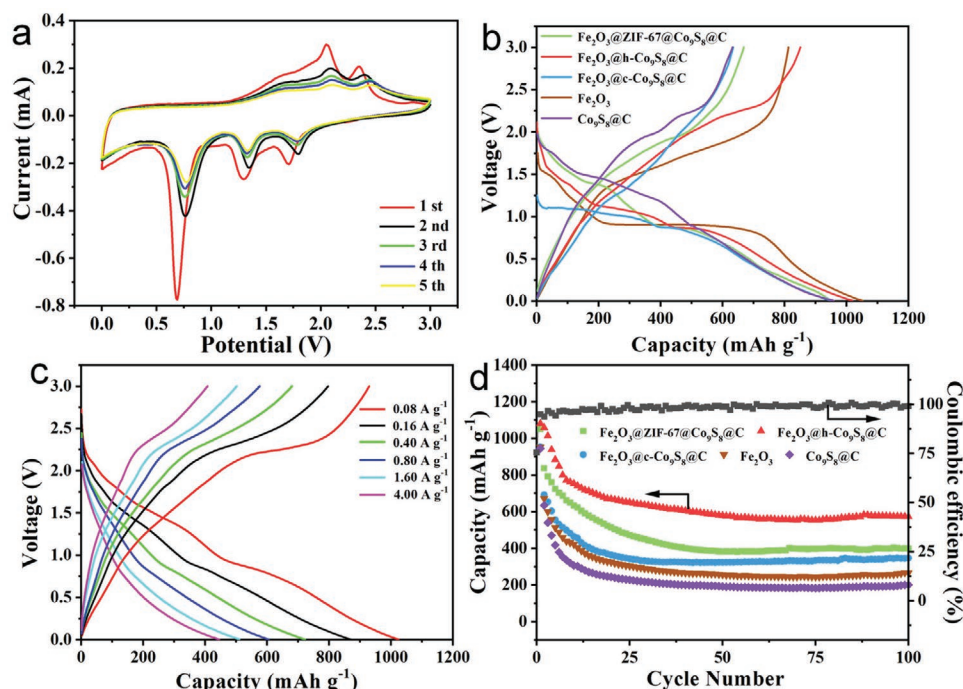

Figure 6. a) CV curves of the Fe_2O_3@h-Co_9S_8@C electrode at a scan rate of 0.1 mV s^{-1} for the 1st–5th cycles. b) The first cycle charge/discharge curves of different materials in the voltage range of 0.01–3.00 V at a current density of 100 mA g^{-1}. c) Charge/discharge curves of Fe_2O_3@h-Co_9S_8@C electrode at various current densities. d) Cycling performance of material electrodes at 1.0 A g^{-1} and Coulombic efficiency of Fe_2O_3@h-Co_9S_8@C.

**ADVANCED
SCIENCE NEWS**
www.advancedsciencenews.com

**NANO · MICRO
small**
www.small-journal.com

and Co^0/Co_9S_8.[9a,31] After the first cycle, the peak shifts positively and the peak intensity decreases, which can be ascribed to the changes in particle size caused by the insertion of Li^+ and the irreversible formation of the solid electrolyte interphase (SEI) layer caused by the decomposition of the electrolyte, respectively.[32] The initial lithiation progress of Fe_2O_3, Co_9S_8, and carbon matrix during the first discharge cycle will take place irreversible structural reorganization to some extent, in accordance with previous studies. For example, by using the in situ transmission electron microscopy, Su et al. found the Fe_2O_3 nanoparticles exhibit volume expansion from the size of 56.0 to 68.2 nm during the lithiation progress, accompanied with morphological changes and formation of nanocrystalline Li_2O.[33] The lithiation mechanism of Co_9S_8 was also investigated by using the in situ TEM in Han's work.[34] The similar volume and morphological changes of Co_9S_8 are attributed to the conversion reaction between Co_9S_8 and Li, along with the metallic Co clusters dispersed in the Li_2S matrix. According to the CV curve and the previous research, the involved electrochemical reaction can be proposed by subsequent equation[9a,30]

$$Fe_2O_3 + 6Li^+ + 6e^- \rightarrow 2Fe + Li_2O \qquad (1)$$

$$Co_9S_8 + 16Li^+ + 16e^- \rightarrow 9Co + 8Li_2S \qquad (2)$$
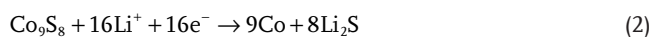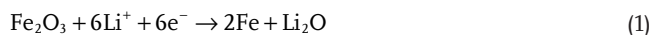
The fluctuation in the CV curve of pure Fe_2O_3 reflects its poor battery stability, and the decrease of $Co_9S_8@C$ CV peaks refer to its attenuate capacity which ascribes to the formation of Li_2S and irreversible volume expansion. By contrast, the CV plot shape of Fe_2O_3–h-$Co_9S_8@C$ remains an overlapping trend, which means that as-prepared material has fine reversibility during the charge/discharge process. It illustrates that the void of yolk–shell Fe_2O_3–h-$Co_9S_8@C$ can accommodate the volume change of Co_9S_8 and the battery performance has been greatly improved. The reduction peak of Fe_2O_3–h-$Co_9S_8@C$ is sharper and stronger than pristine $Co_9S_8@C$ and Fe_2O_3, demonstrating that it has better lithium-ions storage performance than the pristine $Co_9S_8@C$ and Fe_2O_3.

The representative charge/discharge profiles are given in Figure 6b and Figure S13a,b (Supporting Information). The discharge voltage plateau of Fe_2O_3 around 0.85 and 0.4 V corresponds to the reduction reaction of Fe^{3+}/Fe^{2+} and Fe^{2+}/Fe^0. And the voltage plateaus of Co_9S_8 also coincide with the cathodic/anodic peaks in the CV curve. All $Fe_2O_3@Co_9S_8@C$ series materials present two plateaus obviously, the plateau located at the 1.32 V can be ascribed to the Co_9S_8 transform to Co with the formation of Li_2S, the peak location of 0.8 V is caused by the changes of iron valence.

The charge/discharge curves of Fe_2O_3–h-$Co_9S_8@C$ electrode at different current rates are measured to study its high-rate capability (Figure 6c). The Fe_2O_3–h-$Co_9S_8@C$ exhibits stable and reversible capacities of 1024.4, 864.3, 723.8, 600.9, and 511.3 mAh g^{-1} when the current density increased from 0.08, 0.16, 0.40, and 0.80 to 1.60 A g^{-1}. Even at the high current density of 4.0 A g^{-1}, the sample still retains high discharge capacity of 445.2 mAh g^{-1}. It can be seen from Figure 6a,b and Figure S13a,b (Supporting Information) that dual active components of Fe_2O_3 and Co_9S_8 possess different voltage plateaus.

The reduction (oxidation) peaks of Fe_2O_3 locate at 0.4 and 0.85 V (1.5 V), whereas the reduction (oxidation) peaks of Co_9S_8 locate at 1.32 V (0.5 V, 1.4 V). During the lithium-ion batteries cycles, with the synergy effects of Fe_2O_3 and Co_9S_8, the inactive component can serve as a buffer material to alleviate the mechanical strain caused by the lithium intercalation/extraction reaction with another component so that an excellent cyclic structure stability can be acquired as a result.

The cycling performance of different materials is depicted in Figure 6d. The capacity of Fe_2O_3–h-$Co_9S_8@C$ after 100 cycles retains 570.8 mAh g^{-1} at the current density of 1.0 A g^{-1}. The Coulombic efficiency can always maintain above 99.5% after initial many cycles activation. The pure Fe_2O_3 and $Co_9S_8@C$ materials have superior initial capacity, however, the capacity fades away in the first 10 cycles intensely, which can be ascribed to SEI formation and polarization of the electrode. It is proven that the induced electronic effect of yolk–shell structure is able to reinforce the connection between two composites.[35] The introduction of high conductive Co_9S_8 facilitates the conductivity of material effectively and the void space of Fe_2O_3–h-$Co_9S_8@C$ can buffer the volume changes of Co_9S_8 during the cycling process. Consequently, high reversible capacity and good cycle stability are obtained with these merits. Moreover, the cycling behaviors of other samples at different rates are explored (Figure S14a, Supporting Information). The series of $Fe_2O_3@Co_9S_8@C$ materials exhibit the higher capacities at different current densities range from 0.08 to 4.0 A g^{-1}, which displays cheerful rate capability.

To investigate charge transfer kinetics of these materials, the electrochemical impedance spectroscopy (EIS) of materials is performed in Figure S14b–f of the Supporting Information. All samples exhibit a characteristic Nyquist plot consist of a semicircle at the high-frequency region and an inclined line at the low-frequency. The increasing radius of the semicircle is associated with the enlarged charge transfer resistance (R_{ct}), which is consistent with the poor rate performance and fade away of capacity. The Nyquist plots of Fe_2O_3–h-$Co_9S_8@C$ manifest unnoticeable change and smallest semicircle radius comparing with other materials, which means that it possesses the favorable stability and interface transmission rate. Its hollow shell structure can facilitate the infiltration of electrolytes and increase the reaction contact area, thus shorten Li-ion diffusion path and rapid mass/electron transport kinetics are acquired.

According to the previous results and analysis, the excellent electrochemical performance of Fe_2O_3–h-$Co_9S_8@C$ can be attributed to the following merits. First, porous carbon shell and well dispersed Co_9S_8 not only enhance the electrical conductivity of the material, but also provide numerous accessible active sites for electrocatalytic reactions. Second, the electrolyte is apt to penetrate the porous carbon shell, thereby shortening the ion diffusion path and accelerating the reaction kinetics. Third, with the help of synergy effects between Fe_2O_3 and Co_9S_8, the inactive component can serve as a buffer material to alleviate the mechanical strain and preserve the yolk–shell structure during the OER and LIBs cycling. Four, the mechanical and spatial properties of the yolk–shell structure are conducive to good reaction stability reversibility. Hence, Fe_2O_3–h-$Co_9S_8@C$ exhibits excellent OER performance and great potential in the application of LIBs.

3. Conclusions

In summary, uniform Fe_2O_3@h-Co_9S_8@C yolk–shelled structure was rationally prepared through a MOFs-directed strategy. Benefiting from the hollow structure of Fe_2O_3 nanotubes and Co_9S_8 nanocages, the conductive carbon coating as well as the synergy effects between different components, the titled Fe_2O_3@Co_9S_8@C possesses abundant accessible active sites, favorable ionic transfer rate, and exceptional reaction kinetics. In the application of oxygen evolution reaction, Fe_2O_3@h-Co_9S_8@C exhibits a low overpotential of 205 mV at 10 mA cm^{-2} and Tafel slope of 55 mV dec^{-1} as well as excellent OER durability. When employed as anode materials for LIBs, it maintains a reversible capacity of 570.8 mAh g^{-1} at 1.0 A g^{-1} after 100 cycles and delivers a capacity of 445.2 mAh g^{-1} even at high current density of 4.0 A g^{-1}. The strategies of self-sacrificing template to generate the yolk–shell structure can be extended to other transition-metal-base materials, offering a facile method and reference to ameliorate the electrochemical performance for a wider scope of applications.

4. Experimental Section

Synthesis of Fe_2O_3 Nanotube: The Fe_2O_3 hollow nanotubes were prepared by a facile hydrothermal reaction according to the work of Jia et al.[36] Typically, 260 mg of $FeCl_3$ and 6.62 mg of $NH_4H_2PO_4$ were dissolved in 80 mL deionized water. After vigorously stirring, the mixed solution was transferred into a 100 mL Teflon-lined stainless-steel autoclave and heated at 220 °C for 48 h. The suspension was centrifuged and washed several times with ultrapure water and ethanol. Finally, the scarlet Fe_2O_3 nanotubes were obtained by drying the precipitate at 60 °C overnight.

Synthesis of Fe_2O_3@ZIF-67: The Fe_2O_3@ZIF-67 core–shell particles were synthesized via a seed-mediated growth method. In a typical synthesis, 100 mg of Fe_2O_3 nanotubes was added into 50 mL of methanol solution with ultrasonic treatment for 30 min (solution A). Then, 1.20 g of PVP was added into the above solution with vigorously stirring. Meanwhile, 0.4 g of $Co(NO_3)_2$·$6H_2O$ was dissolved in 50 mL of methanol (solution B), and 6.92 g of 2-methylimidazole was dissolved in 100 mL of methanol (solution C). The solution B and solution C were added into solution A simultaneously and stirred at room temperature for 2 h. The precipitate was collected through centrifugation followed by washed with methanol solution and dried in 60 °C overnight.

Synthesis of Fe_2O_3@h-Co_9S_8@C: The fabrication of Fe_2O_3@h-Co_9S_8@C yolk–shell structure involved the initial formation of Fe_2O_3@ZIF-67@a-CoS core–shell structure by sulfidation of ZIF-67 and subsequent annealing treatment under the protection of N_2. Briefly, 120 mg of the as-prepared Fe_2O_3@ZIF-67 was added into 200 mL of isopropanol solution and ultrasound for 10 min. Then, 2 mmol of TAA was added into the above solution. After stirring for 12 h at room temperature, an intermediate with a core–shell structure of Fe_2O_3@ZIF-67@a-CoS was obtained. After washing with isopropanol solution several times, the intermediate was dried at 60 °C in vacuum oven overnight. The Fe_2O_3@Co_9S_8@C nanocomposites were obtained by calcinating the intermediate at 300 °C for 2 h with the ramping rate of 2 °C min^{-1} in the N_2 atmosphere. The amount of TAA exerted an important influence on the composite and morphology of the ZIF-67 templates, which subsequently affected the electrochemical performance of Fe_2O_3@Co_9S_8@C nanocomposites. To obtain optimal electrode materials with high electrochemical performance, 1 and 3 mmol of TAA were used for comparison, and the corresponding products were named as Fe_2O_3@ZIF-67@Co_9S_8@C and Fe_2O_3@c-Co_9S_8@C, respectively. Carbon-coated Co_9S_8 nanocages were also prepared by the same synthesis route without the addition of Fe_2O_3.

Material Characterizations: The phase of the as-prepared samples was analyzed by X-ray diffraction (XRD, Rigaku D/MAX RINT-2000) with Cu Kα radiation (λ = 1.5406 Å) in the 2θ angel from 10° to 80°. The morphology, microstructure, crystal structure, and element distribution were investigated by an FESEM (HITACHI S-4800), TEM (Element mapping, JEOL, JEM2100F) with an accelerating voltage of 200 kV. XPS was recorded on a Thermo ESCALAB 250XI to explore the valence states of elements on the surface of materials. Raman spectra was tested on a Horiba Scientific to study the property of carbon shell. ICP-OES was carried out to investigate the composition on a PerkinElmer 8300.

Electrochemical Measurements: Oxygen evolution reaction performance was tested employing a standard three-electrode system with a CHI660e electrochemical workstation. The catalytic ink was prepared by mixed 3 mg of materials, 55 µL of ethanol, 165 µL of water, and 20 µL of naphthol followed by ultrasonic treatment. Then, 80 µL of the obtained ink was dropped on the nickel foam (NF) evenly and dried in the vacuum oven to prepare the working electrode. A carbon rod and standard Hg/HgO electrode were employed as counter electrode and reference electrode, respectively. All OER related measurements were performed in an alkaline electrolyte (1 M KOH) and corrected with 90% iR compensation to make up for the loss caused by solvent resistance. In the test of LSV and CV, the obtained potentials were converted to the potentials versus reversible hydrogen electrode (RHE) following subsequent equation: $E_{RHE} = E_{(Hg/HgO)} + 0.0592 \times pH + 0.098$. The C_{dl} measurements were performed in the potentials range where was a non-Faradaic current response for each catalyst. The TOF of different materials were calculated with following formula: TOF $= J \times A/(4 \times F \times n)$, in which J is the corresponding current density at different specific overpotential (A cm^{-2}), A is the foam nickel supported catalyst area, which is 1 cm^2 in the study, F is the Faraday constant (96 485 mol C^{-1}), and n is the total number of moles of the active metal sites of the catalyst by assuming that all the Fe and Co atoms are catalytically active in OER.

The electrochemical properties were tested with CR-2032 coin-type half cells assembled in the Argon-filled glove box. The working electrode was prepared by mixing 80 wt% active materials, 10 wt% acetyleneblack, and 10 wt% polyvinylidene fluorides with the solvent of N-methyl pyrrolidone. The as-prepared slurry was added dropwise quantitatively on copper foil and dried in the vacuum oven at 100 °C overnight. The battery was assembled employing lithium foil as reference electrode and 1 M $LiPF_6$ dissolved in 1:1 volume ratio of ethylene carbonate and diethyl carbonate as electrolyte. Galvanostatic charge and discharge tests and lithium storage behavior were tested in the potential window between 0.01 and 3.00 V with the LAND CT2001A battery tester system. CV was carried out at a scan rate of 0.1 mV s^{-1} in an electrochemical workstation (CHI660C). The EIS was obtained with an amplitude of 5 mV in the frequency range of 0.01 Hz–100 kHz.

Supporting Information

Supporting Information is available from the Wiley Online Library or from the author.

Acknowledgements

the Shiyanjia Lab (www.shiyanjia.com) for the XPS tests and the High-Performance Computing Center of Shanghai University and Shanghai Engineering Research Center of Intelligent Computing System (No. 19DZ2252600) for providing the computing resources and technical support.

Conflict of Interest

The authors declare no conflict of interest.

Data Availability Statement

Research data are not shared.

Keywords

chemical etching, energy storage, Fe_2O_3, hollow structure, oxygen evolution reaction

[1] a) C. Y. Yang, J. Chen, X. Ji, T. P. Pollard, X. J. Lu, C. J. Sun, S. Hou, Q. Liu, C. M. Liu, T. T. Qing, Y. Q. Wang, O. Borodin, Y. Ren, K. Xu, C. S. Wang, *Nature* **2019**, *569*, 245; b) C. Liu, J. Qian, Y. F. Ye, H. Zhou, C. J. Sun, C. Sheehan, Z. Y. Zhang, G. Wan, Y. S. Liu, J. H. Guo, S. Li, H. Shin, S. Hwang, T. B. Gunnoe, W. A. Goddard, S. Zhang, *Nat. Catal.* **2021**, *4*, 36; c) H. M. Wang, Z. N. Chen, D. S. Wu, M. N. Cao, F. F. Sun, H. Zhang, H. H. You, W. Zhuang, R. Cao, *J. Am. Chem. Soc.* **2021**, *143*, 4639.

[2] L. L. Li, M. Ye, Y. H. Ding, D. Y. Xie, D. S. Yu, Y. X. Hu, H. Y. Chen, S. J. Peng, *J. Alloys Compd.* **2020**, *812*, 152099.

[3] J. S. Kim, B. Kim, H. Kim, K. Kang, *Adv. Energy Mater.* **2018**, *8*, 1702774.

[4] a) B. Ye, L. R. Huang, Y. P. Hou, R. H. Jiang, L. Sun, Z. B. Yu, B. G. Zhang, Y. Y. Huang, Y. L. Zhang, *J. Mater. Chem. A* **2019**, *7*, 11379; b) J. Kong, A. Lim, C. Yoon, J. H. Jang, H. C. Ham, J. Han, S. Nam, D. Kim, Y. E. Sung, J. Choi, H. S. Park, *ACS Sustainable Chem. Eng.* **2017**, *5*, 10986; c) Y. W. Li, Y. Huang, Y. Y. Zheng, R. S. Huang, J. H. Yao, *J. Power Sources* **2019**, *416*, 62; d) F. Li, G. E. Luo, W. Y. Chen, Y. C. Chen, Y. P. Fang, M. T. Zheng, X. Y. Yu, *ACS Appl. Mater. Interfaces* **2019**, *11*, 36949.

[5] F. X. Ma, H. Hu, H. Bin Wu, C. Y. Xu, Z. C. Xu, L. Zhen, X. W. Lou, *Adv. Mater.* **2015**, *27*, 4097.

[6] P. L. Zheng, Y. Zhang, Z. F. Dai, Y. Zheng, K. N. Dinh, J. Yang, R. Dangol, X. B. liu, Q. Y. Yan, *Small* **2018**, *14*, 1704065.

[7] B. H. R. Suryanto, Y. Wang, R. K. Hocking, W. Adamson, C. Zhao, *Nat. Commun.* **2019**, *10*, 5599.

[8] J. Wang, H. He, Z. X. Wu, J. N. Liang, L. L. Han, H. L. L. Xin, X. Y. Guo, Y. Zhu, D. L. Wang, *J. Power Sources* **2018**, *392*, 193.

[9] a) J. Liu, C. Wu, D. D. Xiao, P. Kopold, L. Gu, P. A. van Aken, J. Maier, Y. Yu, *Small* **2016**, *12*, 2354; b) B. C. Qiu, Q. H. Zhu, M. M. Du, L. G. Fan, M. Y. Xing, J. L. Zhang, *Angew. Chem., Int. Ed.* **2017**, *129*, 2728; c) Z. L. Chen, M. Liu, R. B. Wu, *J. Catal.* **2018**, *361*, 322; d) P. Y. Zeng, J. W. Li, M. Ye, K. F. Zhuo, Z. Fang, *Chem. - Eur. J.* **2017**, *23*, 9517.

[10] G. D. Moon, *Nanomaterials* **2020**, *10*, 675.

[11] Q. Q. Xu, W. Huo, S. S. Li, J. H. Fang, L. Li, B. Y. Zhang, F. Zhang, Y. X. Zhang, S. W. Li, *Appl. Surf. Sci.* **2020**, *533*, 147368.

[12] V. Ganesan, J. Son, J. Kim, *Nanoscale* **2021**, *13*, 4569.

[13] a) Q. Qin, L. L. Chen, T. Wei, X. E. Liu, *Small* **2019**, *15*, 1803639; b) Z. Li, Y. J. Fang, J. T. Zhang, X. W. Lou, *Adv. Mater.* **2018**, *30*, 1800525; c) J. H. Shi, F. Qiu, W. B. Yuan, M. M. Guo, Z. H. Lu, *Chem. Eng. J.* **2021**, *403*, 126312.

[14] a) B. Wang, Y. Z. Ye, L. Xu, Y. Quan, W. X. Wei, W. S. Zhu, H. M. Li, J. X. Xia, *Adv. Funct. Mater.* **2020**, *30*, 2005834; b) X. Y. Li, Y. Y. Ma, G. Z. Cao, Y. Q. Qu, *J. Mater. Chem. A* **2016**, *4*, 12487.

[15] Y. Pan, K. A. Sun, S. J. Liu, X. Cao, K. L. Wu, W. C. Cheong, Z. Chen, Y. Wang, Y. Li, Y. Q. Liu, D. S. Wang, Q. Peng, C. Chen, Y. D. Li, *J. Am. Chem. Soc.* **2018**, *140*, 2610.

[16] H. Hu, L. Han, M. Z. Yu, Z. Y. Wang, X. W. Lou, *Energy Environ. Sci.* **2016**, *9*, 107.

[17] W. Shuang, L. J. Kong, M. Zhong, D. H. Wang, J. Liu, X. H. Bu, *Dalton Trans.* **2018**, *47*, 12385.

[18] Y. Li, K. Zhou, M. He, J. F. Yao, *Microporous Mesoporous Mater.* **2016**, *234*, 287.

[19] a) J. Ouyang, Z. Zhao, S. L. Suib, H. M. Yang, *J. Colloid Interface Sci.* **2019**, *539*, 135; b) H. L. Wang, B. F. Jin, H. B. Wang, N. N. Ma, W. Liu, D. Weng, X. D. Wu, S. Liu, *Appl. Catal., B* **2018**, *237*, 251.

[20] a) W. T. Wei, L. W. Mi, Y. Gao, Z. Zheng, W. H. Chen, X. X. Guan, *Chem. Mater.* **2014**, *26*, 3418; b) P. Ganesan, M. Prabu, J. Sanetuntikul, S. Shanmugam, *ACS Catal.* **2015**, *5*, 3625.

[21] X. Lu, X. Chen, W. Zhou, Y. Tong, G.-R. Li, *ACS Appl. Mater. Interfaces* **2015**, *7*, 14843.

[22] G. Yilmaz, K. M. Yam, C. Zhang, H. J. Fan, G. W. Ho, *Adv. Mater.* **2017**, *29*, 1606814.

[23] W. J. Jiang, T. Tang, Y. Zhang, J. S. Hu, *Acc. Chem. Res.* **2020**, *53*, 1111.

[24] S. L. Zhao, Y. Wang, J. C. Dong, C. T. He, H. J. Yin, P. F. An, K. Zhao, X. F. Zhang, C. Gao, L. J. Zhang, J. W. Lv, J. X. Wang, J. Q. Zhang, A. M. Khattak, N. A. Khan, Z. X. Wei, J. Zhang, S. Q. Liu, H. J. Zhao, Z. Y. Tang, *Nat. Energy* **2016**, *1*, 1.

[25] C. C. L. McCrory, S. Jung, I. M. Ferrer, S. M. Chatman, J. C. Peters, T. F. Jaramillo, *J. Am. Chem. Soc.* **2015**, *137*, 4347.

[26] N. Zhang, Q. Zhang, C. Xu, Y. Li, J. Y. Zhang, L. Wu, Y. F. Liu, Y. Z. Fang, Z. F. Liu, *Chem. Eng. J.* **2021**, *426*, 131192.

[27] a) H. Li, Z. Guo, X. W. Wang, *J. Mater. Chem. A* **2017**, *5*, 21353; b) X. T. Feng, Q. Z. Jiao, T. Liu, Q. Li, M. M. Yin, Y. Zhao, H. S. Li, C. H. Feng, W. Zhou, *ACS Sustainable Chem. Eng.* **2018**, *6*, 1863.

[28] Q. Q. Xu, W. Huo, S. S. Li, J. H. Fang, L. Li, B. Y. Zhang, F. Zhang, Y. X. Zhang, S. W. Li, *Appl. Surf. Sci.* **2020**, *533*, 147368.

[29] a) W. Chen, H. T. Wang, Y. Z. Li, Y. Y. Liu, J. Sun, S. H. Lee, J. S. Lee, Y. Cui, *ACS Cent. Sci.* **2015**, *1*, 244; b) O. Mabayoje, A. Shoola, B. R. Wygant, C. B. Mullins, *ACS Energy Lett.* **2016**, *1*, 195.

[30] Z. Y. Li, Y. N. Mao, Q. H. Tian, W. Zhang, L. Yang, *J. Alloys Compd.* **2019**, *784*, 125.

[31] J. Wang, S. H. Ng, G. X. Wang, J. Chen, L. Zhao, Y. Chen, H. K. Liu, *J. Power Sources* **2006**, *159*, 287.

[32] a) D. Di Lecce, R. Verrelli, D. Campanella, V. Marangon, J. Hassoun, *ChemSusChem* **2017**, *10*, 1607; b) S. K. Park, G. D. Park, Y. C. Kang, *Nanoscale* **2018**, *10*, 11150.

[33] Q. M. Su, D. Xie, J. Zhang, G. H. Du, B. S. Xu, *ACS Nano* **2013**, *7*, 9115.

[34] S. B. Han, Y. M. Zhu, C. Cai, J. K. Zhu, W. B. Han, L. Chen, X. T. Zu, H. Yang, M. Gu, *Appl. Phys. Lett.* **2019**, *114*, 113901.

[35] S. F. Kong, R. L. Dai, H. Li, W. W. Sun, Y. Wang, *ACS Sustainable Chem. Eng.* **2015**, *3*, 1830.

[36] C. J. Jia, L. D. Sun, Z. G. Yan, L. P. You, F. Luo, X. D. Han, Y. C. Pang, Z. Zhang, C. H. Yan, *Angew. Chem., Int. Ed.* **2005**, *44*, 4328.